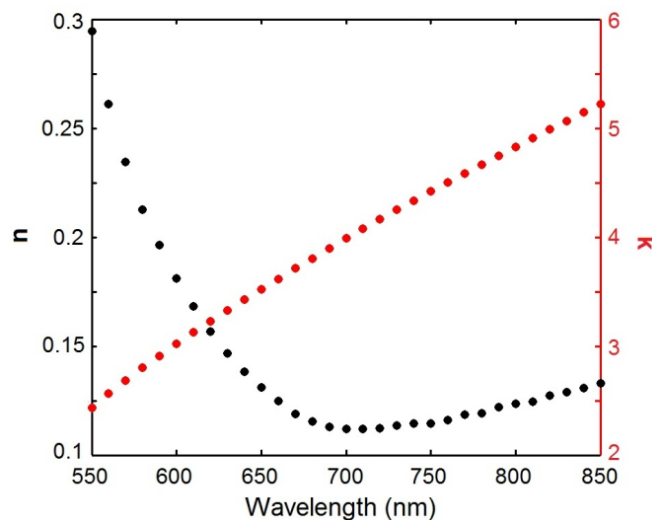


Electronic supplementary material (ESI) for Lab on a Chip

## Plasmonic interferometric sensor arrays for high-performance label-free biomolecular detection

Yongkang Gao,<sup>a</sup> Zheming Xin,<sup>a</sup> Beibei Zeng,<sup>a</sup> Qiaoqiang Gan,<sup>b</sup> Xuanhong Cheng<sup>c</sup> and Filbert J. Bartoli<sup>\*a</sup>

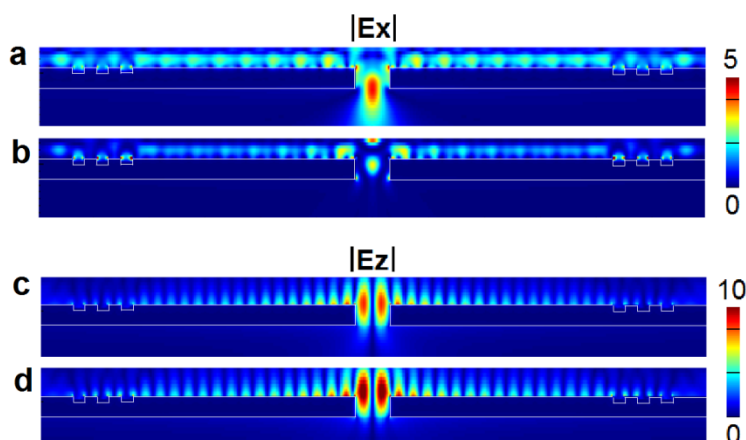
### 1. Measured optical constants of gold film.



**Fig. S1.** Measured  $n$  and  $k$  of the gold film used in the experiments. Measured by J. A. Woollam, V-VASE ellipsometer.

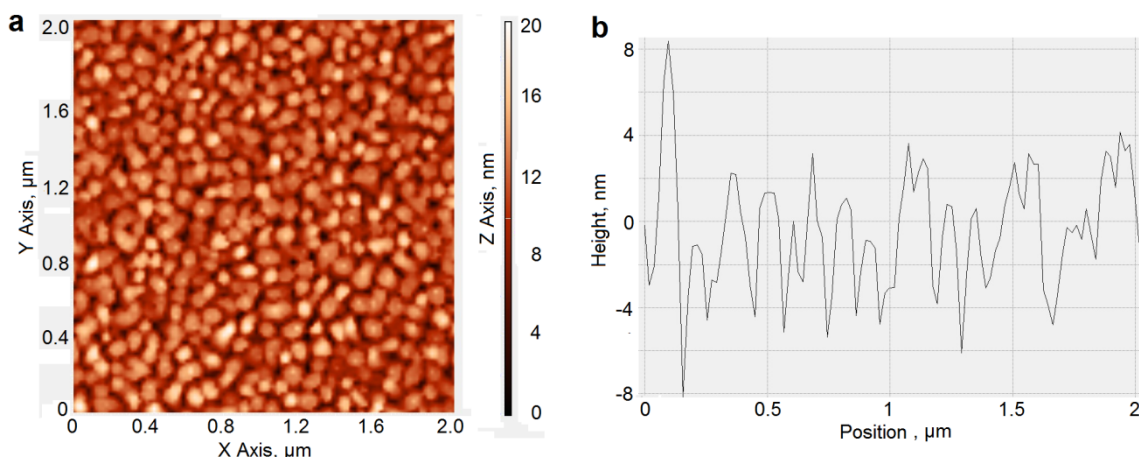
### 2. Electric field distributions.

Fig. S2. shows the calculated field distributions of  $|E_x|$  and  $|E_z|$  components, respectively. From the field distributions it is clear that  $|E_x|$  component plays a dominant role in determining the enhanced light transmission and suppression through the interferometer structures.



**Fig. S2.** Calculated  $|E_x|$  distributions at interference peak (a) and valley (b) wavelengths. Calculated  $|E_z|$  distributions at interference peak (c) and valley (d) wavelengths.

### 3. Atomic force microscopy (AFM) images of the gold sample surface.



**Fig. S3.** AFM images of a 300 nm gold film. The root mean square roughness is 2.9 nm, measured from a  $2 \times 2 \mu\text{m}^2$  area using a NT-MDT Solver NEXT AFM.

#### 4. Transmission spectra of interferometers with different number of circular grooves.

Fig. S3a shows the transmission spectra of the interferometer arrays with different number of circular grooves. For interferometer array with three circular grooves, the interference contrast  $C$  reaches the highest value of 0.87. While further increase of the groove number causes the transmitted intensity to increase, the interference contrast decreases. For interferometers with groove number of 1, 2, 3, 4, 5, and 6, the interference contrasts are 0.56, 0.81, 0.87, 0.84, 0.78, and 0.75, respectively.

We now further discuss the origin of such contrast dependence on groove numbers. Since each groove in a circular groove array can excite SPPs but has a different distance to the central aperture, the SPP phase delay from each groove to the aperture is different and leads to slightly different interference patterns. We treat the interference pattern of the hole-grating structure approximately as a superposition of the contributions from each groove. Fig. S3b shows the interference fringes (calculated using eq 1) resulting from each groove (green curves) and their superposition (the red curve). It is clear that as the groove number increases from 3 to 5, and to 7, the transmission increases at the valley position (indicated by the black arrows), and accordingly, the interference contrast decreases.

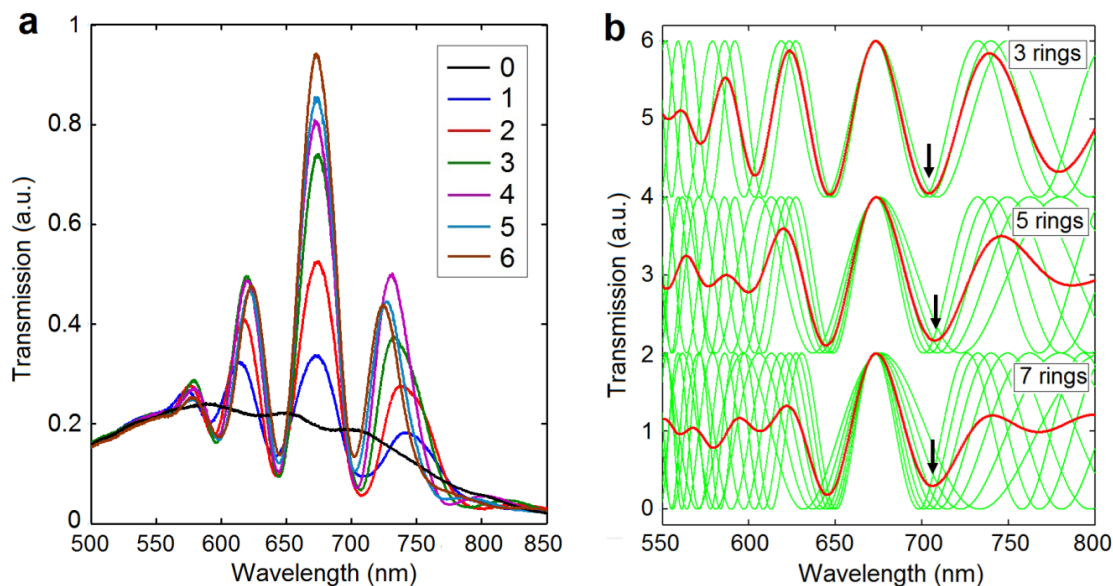


**Fig. S4.** (a) Transmission spectra for interferometers with increasing number of circular grooves from 0 to 6. (b) Analytically calculated interference patterns contributed by each groove (the green curves) and their superposed interference fringe (the red curve).

#### 5. Time resolution vs sensor RIU resolution.

An easy and efficient way to enhance the resolution of a plasmonic sensor using spectral modulation is to increase the number of spectra averaged, but at the cost of time resolution. For real-time kinetics measurement, care must be taken to balance such trade-off between time and sensor resolution. In this work, 200 spectra were averaged and yielded a time resolution of 10 s (50 ms integration time for each spectrum). For even faster kinetics measurement, a smaller number of spectra can be averaged with a modest increase in the sensor noise level (see Fig. S5).

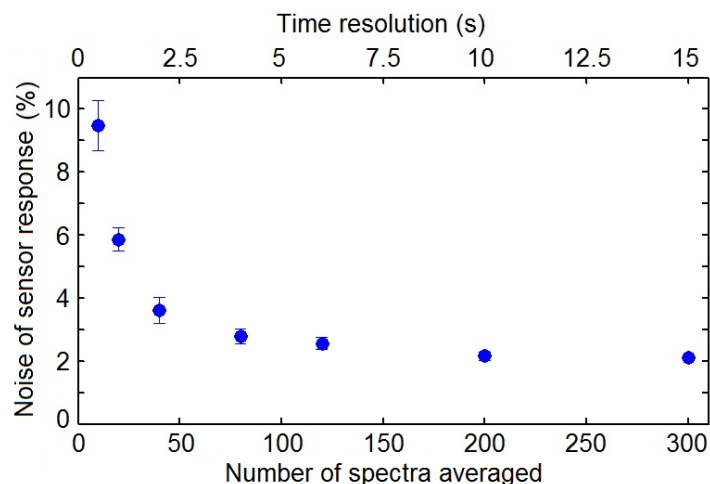


Fig. S5. The sensor noise for different number of spectra averaged.

### 6. Single-peak tracking method.

For the conventional single-peak monitoring method, the spectral position of the interference peak at 674.5 nm in Figure 3a was recorded in real time by using a Lorentzian fitting method (see Fig. S4a). The peak position was then extracted and plotted in Figure S4b as a function of the liquid refractive index. The slope of the linear fit to the data points gives the sensor sensitivity of 470.6 nm/RIU. The inset of Figure S4a indicates the noise level of the sensor response. The standard deviation of the monitored peak position is  $7.3 \times 10^{-4}$  nm, which corresponds to a sensor resolution of  $1.55 \times 10^{-6}$  RIU (i.e.,  $7.3 \times 10^{-4}$  nm/470.6 nm/RIU).

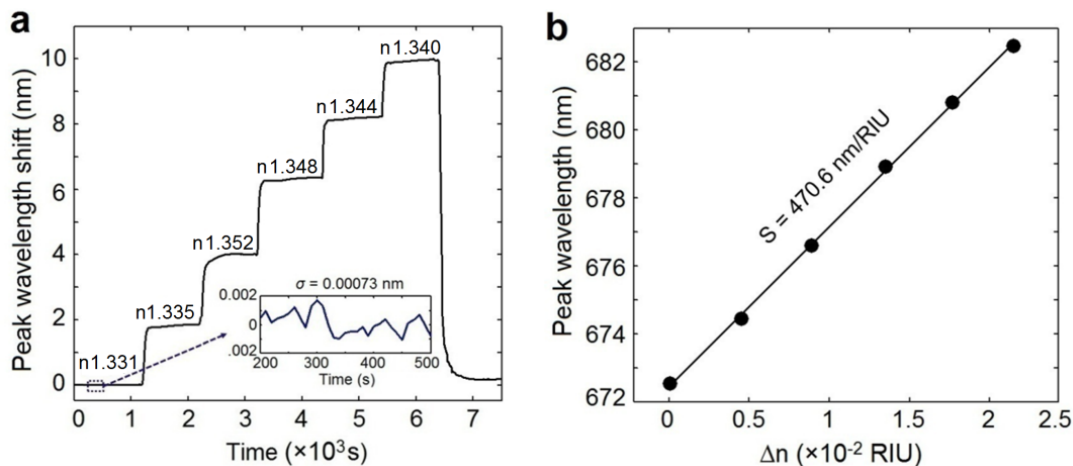
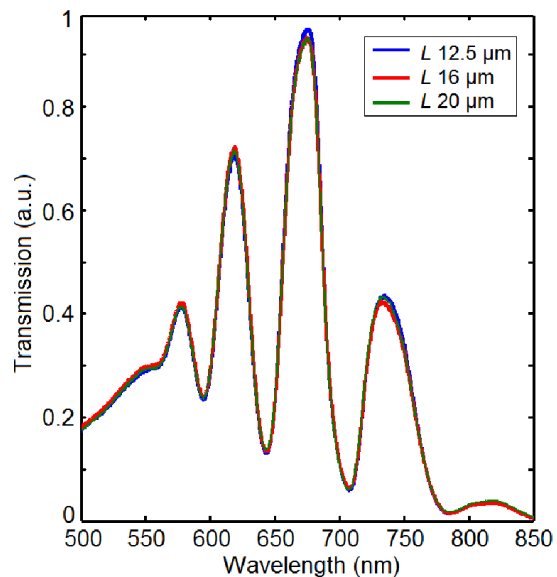


Fig. S6. (a) The monitored interference peak position as a function of time. The lower inset shows the standard deviation of the sensor response. (b) The extracted peak position as a function of liquid refractive index.

### 7. Crosstalk between sensing pixels.

The crosstalk between sensing pixels in our sensor array is minimal for two reasons. First, the circular grooves serve as both efficient SPP couplers and Bragg mirrors to block SPPs from adjacent sensing pixels. Second, the circular structure design ensures SPPs propagate radially towards adjacent structures. This allows only a very limited portion of SPPs propagate towards the hole locations of surrounding sensors and lead to unwanted cross-talk. To verify this hypothesis, we measured the spectra of sensor arrays with increasing sensor-to-sensor distance  $L$  from 12.5 to 20  $\mu\text{m}$

(see Fig. S7). There is no obvious difference between collected spectra, demonstrating the minimal crosstalk between sensing pixels. This unique feature is especially useful for high-throughput multiplexed sensing as sensors can be more densely packed on a chip.



**Fig. S7.** The transmission spectra for sensor arrays with different sensor-to-sensor distances.